ARTICLE

Fluorinated MOF platform for selective removal and sensing of SO_2 from flue gas and air

M.R. Tchalala[1], P.M. Bhatt [1], K.N. Chappanda[2], S.R. Tavares[3], K. Adil [1], Y. Belmabkhout [1], A. Shkurenko [1], A. Cadiau[1], N. Heymans[4], G. De Weireld[4], G. Maurin[3], K.N. Salama [2] & M. Eddaoudi [1]

Conventional SO_2 scrubbing agents, namely calcium oxide and zeolites, are often used to remove SO_2 using a strong or irreversible adsorption-based process. However, adsorbents capable of sensing and selectively capturing this toxic molecule in a reversible manner, with in-depth understanding of structure–property relationships, have been rarely explored. Here we report the selective removal and sensing of SO_2 using recently unveiled fluorinated metal–organic frameworks (MOFs). Mixed gas adsorption experiments were performed at low concentrations ranging from 250 p.p.m. to 7% of SO_2. Direct mixed gas column breakthrough and/or column desorption experiments revealed an unprecedented SO_2 affinity for KAUST-7 (NbOFFIVE-1-Ni) and KAUST-8 (AlFFIVE-1-Ni) MOFs. Furthermore, MOF-coated quartz crystal microbalance transducers were used to develop sensors with the ability to detect SO_2 at low concentrations ranging from 25 to 500 p.p.m.

[1] Functional Materials Design, Discovery and Development Research Group (FMD³), King Abdullah University of Science and Technology (KAUST), Thuwal 23955-6900, Saudi Arabia. [2] Sensors Lab, Advanced Membranes and Porous Materials Center, Division of Physical Sciences and Engineering, King Abdullah University of Science and Technology (KAUST), Thuwal 23955-6900, Saudi Arabia. [3] Institut Charles Gerhardt Montpellier (UMR CNRS 5253), Université Montpellier, Place Eugène Bataillon, 34095 Montpellier, Cedex 05, France. [4] Service de thermodynamique, Faculté Polytechnique de Mons, Université de Mons, 20 Place du Parc, B-7000 Mons, Belgium. These authors contributed equally: M. R. Tchalala, P. M. Bhatt. Correspondence and requests for materials should be addressed to K.N.S. (email: khaled.salama@kaust.edu) or to M.E. (email: mohamed.eddaoudi@kaust.edu)

Global warming and other environmental/ecological issues have forced our society to adopt stringent rules for industrial waste and be on the lookout for ways to improve indoor and outdoor air quality, including in industrial sites. One major form of industrial waste with an adverse effect on the environment is flue gas. Flue gas generated by large industries and power plants resulting from burning fossil fuel contains CO_2 (at a low percent concentration), SO_2 (500–2000 p.p.m.), NO_2 (few p.p.m.), water vapor, and nitrogen (as the dominant gas)[1]. Although the concentration of SO_2 in flue gas feed is low, it could be poisonous for most liquid- or/and solid-state-based CO_2 separating agents. Therefore, the removal of SO_2 from flue gas is of prime importance[2]. Current SO_2 removal technology involves the irreversible acid–base reaction of SO_2 with CaO to form $CaSO_3$[3]. The main drawback of this technology is its relatively low removal efficiency (< 90%) associated with an almost impossible regeneration step due to its extremely energy-intensive cost. Therefore, cyclable physical sorption technology is perceived as an effective alternative approach. Hence, identification of an adsorbent that can efficiently capture SO_2, particularly at low concentration (< 500 p.p.m.), is crucial.

When SO_2 is not controlled and is emitted into the atmosphere, it has adverse effects on the environment, such as acid rain, and must be monitored[4,5]. Therefore, it is necessary to find efficient solutions to sense SO_2 at p.p.m. level (above 25 p.p.m.) in both dry and humid conditions. Recently, there have been considerable efforts in developing SO_2 sensing devices based on metal oxides (such as SnO_2, WO_3, and TiO_2) due to their excellent sensitivity, selectivity, response time, and recovery time[6–10]. However, most of the semiconductor-based SO_2 sensors were reported to require high temperatures (200–600 °C), leading to high levels of power consumption[11–15]. There is therefore a need for gas sensors that operate at room temperature (RT)[16–18], which would be an important parameter and invaluable milestone for developing alternate materials suitable for detecting SO_2.

Metal–organic frameworks (MOFs), one of the most recent classes of porous materials, have attracted immense interest due to their potential to address many enduring challenges pertaining to various key applications[19–21] such as separation, storage, catalysis, and sensing[22–24]. Although many of these MOFs possess good-to-excellent chemical stability (which is a prerequisite for practical industrial applications)[25,26], there are only a few examples of SO_2 adsorption on MOFs, mainly due to its corrosive nature[27–36]. Many of these reported MOFs adsorb SO_2 irreversibly or undergo phase transformations and they are not suitable for SO_2–structural-adsorption-sensing relationships studies; only a handful of MOFs are proven for cyclic stability and SO_2 capture at flue gas concentration[27–30]. In addition, designing a sensor device for reversible SO_2 sensing at p.p.m. level and in the presence of atmospheric moisture is still an ongoing challenge.

Here we report the use of isostructural fluorinated MOFs for (i) selective removal of SO_2 from synthetic flue gas and (ii) sensing of SO_2[37,38] using a quartz crystal microbalance (QCM) as a transducer[18,39–41], as the coating of MOFs on the QCM electrodes can detect the change in mass of sub-nanograms upon adsorption or desorption of molecules by the MOF layer[42,43]. We unveiled an unprecedented concurrent removal of SO_2/CO_2 from synthetic flue gas and remarkable detection capability in p.p.m. level of SO_2 concentration in both dry and humid conditions.

Results

SO_2 removal from flue gas. Recently, our exploration of fluorinated MOF platforms, namely KAUST-7 ([Ni(NbF$_5$)(pyrazine)$_2$]·2H$_2$O, apparent surface area 280 m^2 g^{-1}, estimated pore volume 0.095 cm^3 g^{-1}) and KAUST-8 ([Ni(AlF$_5$(OH$_2$))

(pyrazine)$_2$]·2H$_2$O, apparent surface area 258 m^2 g^{-1}, estimated pore volume 0.102 cm^3 g^{-1}), resulted in many desirable properties that include direct air capture[44], propane-propylene separation[45], gas/vapor dehydration[46], and acid gas (H_2S, CO_2) removal[47]. Although both of the MOFs are isostructural, the subtle differences in their chemical compositions, pillared by the inorganic moiety (NbOF$_5$)$^{2-}$ instead of (AlF$_5$(OH$_2$))$^{2-}$, allowed the modulation of their properties by varying the content and intermolecular spacing of pending fluoride groups realized via different tilts of pyrazine molecules (Fig. 1). Inspired by the excellent stability and the modular nature of these MOF materials[44–46], we investigated their SO_2 removal and sensing in synthetic flue gas and air, respectively.

KAUST-7 was first investigated for SO_2 sorption, which is also one of the best physisorbent materials for capturing CO_2 at atmospheric concentration[44] with good water stability[45]. The steep, pure SO_2 adsorption isotherm collected at 25 °C (Supplementary Figure 1) suggested a high affinity of the KAUST-7 framework for SO_2. To gain better insight on the SO_2 position within the framework and the governing interactions responsible for resultant strong affinity, we performed in situ single crystal X-ray diffraction (SCXRD) study on a suitable single crystal of KAUST-7 at 296 K under 4–5 bar of SO_2-containing atmosphere (7% SO_2, 93% N_2). The structure analysis revealed that the resultant compound crystallized in the tetragonal space group $P4/nbm$ with the unit cell parameters $a = b = 9.9249(2)$ Å and $c = 7.8387(2)$ Å (Supplementary Table 1). An axial distortion of the octahedral (NbOF$_5$)$^{2-}$ anion (Nb–O bond is shorter than Nb–F$_{trans}$, 1.82(3) and 2.03(3) Å, respectively) was observed and manifested in a disorder in the structure: the Nb atom was split over two positions, whereas the oxygen and the $trans$-fluoride were refined in the same position with equal thermal parameters (Supplementary Figure 2a). The fluorinated pillars are turned by $\varphi = \pm 8.5(2)°$ from the direction toward the center of the channel (Supplementary Figure 2b) depending on the central atom position. The (NbOF$_5$)$^{2-}$ anion twist is stabilized by four pairs of C–H···F hydrogen bonds with the adjacent pyrazine molecules: the H···F distances and C–H···F angles are 2.45 Å and 158° in the case of the Nb shifted toward that Ni(pyrazine)$_2$ layer, and 2.52 Å and 170° when in the opposite direction (Supplementary Figure 2c and 2d). The SO_2 molecule was localized in the center of the one-dimensional (1D) channel at a special position, similar to CO_2 molecule in the KAUST-7 (CO_2) structure[44]. As the site symmetry ($-42m$) is higher than the symmetry of the guest molecule, the SO_2 is disordered over four positions around axis -4 with the total occupancy refined to 0.424(4). Contrary to the linear CO_2 molecule surrounded by four F-pillars, the electropositive sulfur atom of the triangular SO_2 molecule interacts with only two electronegative fluorine atoms of the adjacent (NbOF$_5$)$^{2-}$ anions (S···F distances of 2.80(1) and 2.86(1) Å) shown in Fig. 2a–c. In addition, the SO_2 molecule in the MOF is stabilized by four C–H···O contacts with the hydrogen atoms of four different pyrazines (H···O distance = 2.87 Å, angle = 120°).

This observation is corroborated by density functional theory (DFT) calculations, which revealed high SO_2/KAUST-7 interaction energy of -64.8 kJ mol^{-1}. This is due to a relatively stronger interaction between the sulfur atom of SO_2 and the F-pillars with characteristic interatomic distances of 2.9 Å (Supplementary Figure 3a) along with a charge transfer between the guest and this region of the MOF. Interestingly, the SO_2/KAUST-7 interaction energy is as high as the value calculated for CO_2 (-54.5 kJ mol^{-1}). This latter molecule occupies slightly different sites than SO_2, implying an interaction of the guest molecule with both the F-pillars and the pyrazine groups (Supplementary Figure 3b). The so-predicted energetics and spatial distributions
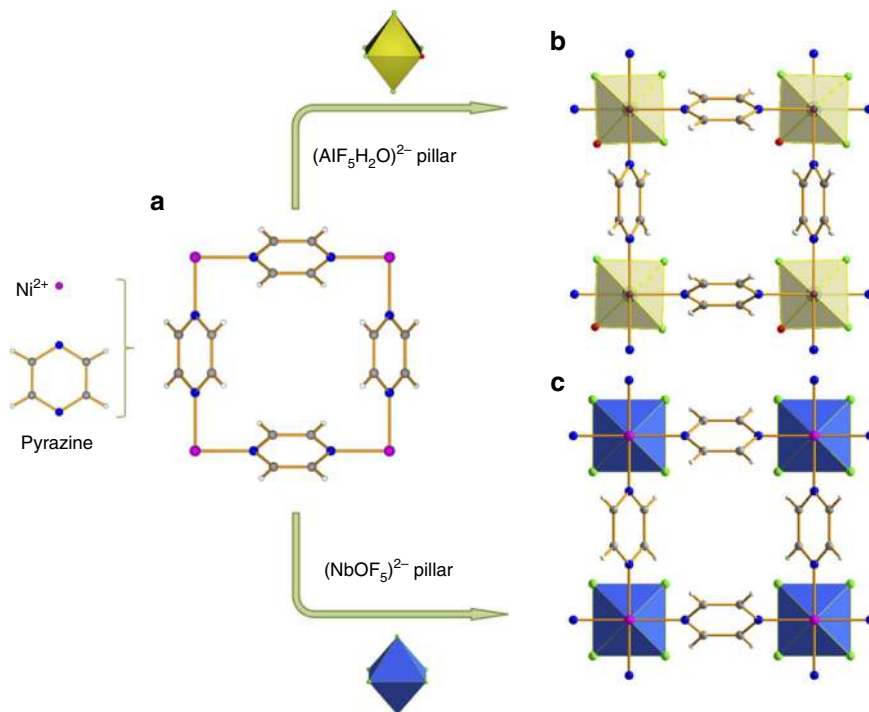
Fig. 1 Synthesis and crystal structure of KAUST-7 and KAUST-8. **a** [Ni(pyrazine)$_2$]$^{2+}$ square grid resulting from the connection of Ni^{2+} cations and pyrazine molecules. **b** Crystal structure of KAUST-8 resulting from the pillaring of [Ni(pyrazine)$_2$]$^{2+}$ square grid with (AlF$_5$(OH$_2$))$^{2-}$ pillar. **c** Crystal structure of KAUST-7 resulting from the pillaring of [Ni(pyrazine)$_2$]$^{2+}$ square grid with (NbOF$_5$)$^{2-}$ pillar

for both molecules as single components suggest simultaneous capture of SO$_2$ and CO$_2$.

Cyclic adsorption column breakthrough tests with SO$_2$/N$_2$: 7/93 indicate stability and good uptake ($\approx$2.2 mmol g^{-1}) of SO$_2$ (Fig. 3a). Furthermore, adsorption column breakthrough experiments with SO$_2$/CO$_2$/N$_2$: 4/4/92 gas mixture showed simultaneous and equal retention time in the column for SO$_2$ and CO$_2$, demonstrating identical uptake of $\approx$1.1 mmol g^{-1} (Supplementary Figure 4), which is consistent with the simulated energetics trends. Upon decreasing the SO$_2$ concentration with nitrogen in the range commonly observed in flue gas (500 p.p.m.) (SO$_2$/N$_2$: 0.05/99.95 mixture) and the immediately dangerous to life or health concentration (100 p.p.m.), KAUST-7 still maintains a high SO$_2$ uptake of about 1.4 mmol g^{-1} at 500 p.p.m. SO$_2$ concentration (Fig. 3b). Interestingly, adsorption column breakthrough experiments under mimicked flue gas conditions with 500 p.p.m. of SO$_2$ and 10% CO$_2$ in N$_2$ (SO$_2$/CO$_2$/N$_2$: 0.05/10/ 89.95) resulted in equal and simultaneous retention time for both SO$_2$ and CO$_2$, leading to uptakes of $\approx$0.01 mmol g^{-1} and $\approx$2.2 mmol g^{-1}, respectively (Fig. 3c). The direct co-adsorption experiments with different SO$_2$ and CO$_2$ compositions (4% SO$_2$, 4% CO$_2$, balance N$_2$ and 500 p.p.m. SO$_2$, 10% CO$_2$, balance N$_2$) demonstrate that KAUST-7 exhibits equal selectivity toward SO$_2$ and CO$_2$ (SO$_2$/CO$_2$ selectivity $\approx$1), which is desirable for simultaneous CO$_2$ and SO$_2$ capture in flue gas (containing low SO$_2$ concentrations). Nevertheless, temperature-programmed desorption (TPD) confirmed the presence of CO$_2$ only with an undetectable amount of SO$_2$ (Fig. 3d) in the adsorbed phase as the amount of SO$_2$ adsorbed is negligible owing to its low concentration. The performance of KAUST-7 using humid ($\approx$40% Relative Humidity (RH)) 250 p.p.m. SO$_2$/balance N$_2$ gas mixture was also investigated (Supplementary Figure 5); it is evident that SO$_2$ has same breakthrough time as that of water and results in a lower SO$_2$ uptake under humid condition compared with the dry condition, which is not surprising

considering the concentration of water is around 50 times higher than that of SO$_2$. In addition to previously reported excellent water stability[44,45], SO$_2$ stability of the KAUST-7 was proven by powder X-ray diffraction (PXRD) comparison of the materials before and after dry and humid SO$_2$ exposure (Supplementary Figure 6), CO$_2$ breakthrough study before and after 7% SO$_2$ breakthrough experiments (Supplementary Figure 7), and CO$_2$ adsorption isotherm after the humid SO$_2$ breakthrough experiment (Supplementary Figure 8).

In our quest for a material with a more favorable selectivity for SO$_2$ removal from flue gas than CO$_2$ (at 500 p.p.m. of SO$_2$), we opted to investigate an analog of KAUST-7 with lower CO$_2$ interactions and potentially higher SO$_2$ interactions. Inspired by our results with KAUST-8 for dehydration of gases[46] and simultaneous removal of H$_2$S/CO$_2$[47], we found it compelling to explore the structural SO$_2$/CO$_2$ co-adsorption property. KAUST-8 exhibits three pendant fluoride groups with slightly higher F…F distance (3.613 Å) and one potential open metal site, whereas KAUST-7 contains four pendants fluoride with smaller F…F distance (3.210(8) Å) and no open metal site. Such minute differences in structural features led us to realize equal selectivity for CO$_2$ and H$_2$S over a wide range of concentrations and temperatures[47]. Encouraged by this structure–property tuning of H$_2$S and CO$_2$ adsorption affinity using this MOF, we expected KAUST-8 to be more selective toward SO$_2$ than CO$_2$. Similar to gain better insight of the KAUST-8 system, SCXRD data were collected on the SO$_2$-loaded KAUST-8 crystal. The structure analysis revealed the resultant compound crystallized in the tetragonal space group P4/mmm with the unit cell parameters $a = b = 6.9996(2)$ Å and $c = 7.7033(2)$ Å (Fig. 2b–d, Supplementary Table 2). Contrary to KAUST-7, a rotational disorder of the (AlF$_5$)$^{2-}$ is caused by trigonal bipyramidal shape of the anions located at the axis 4 among four 1D channels in the structure. When one fluorine atom of a pillar is directed perfectly to the channel center ($\varphi = 0°$), in the two other adjacent channels Al–F

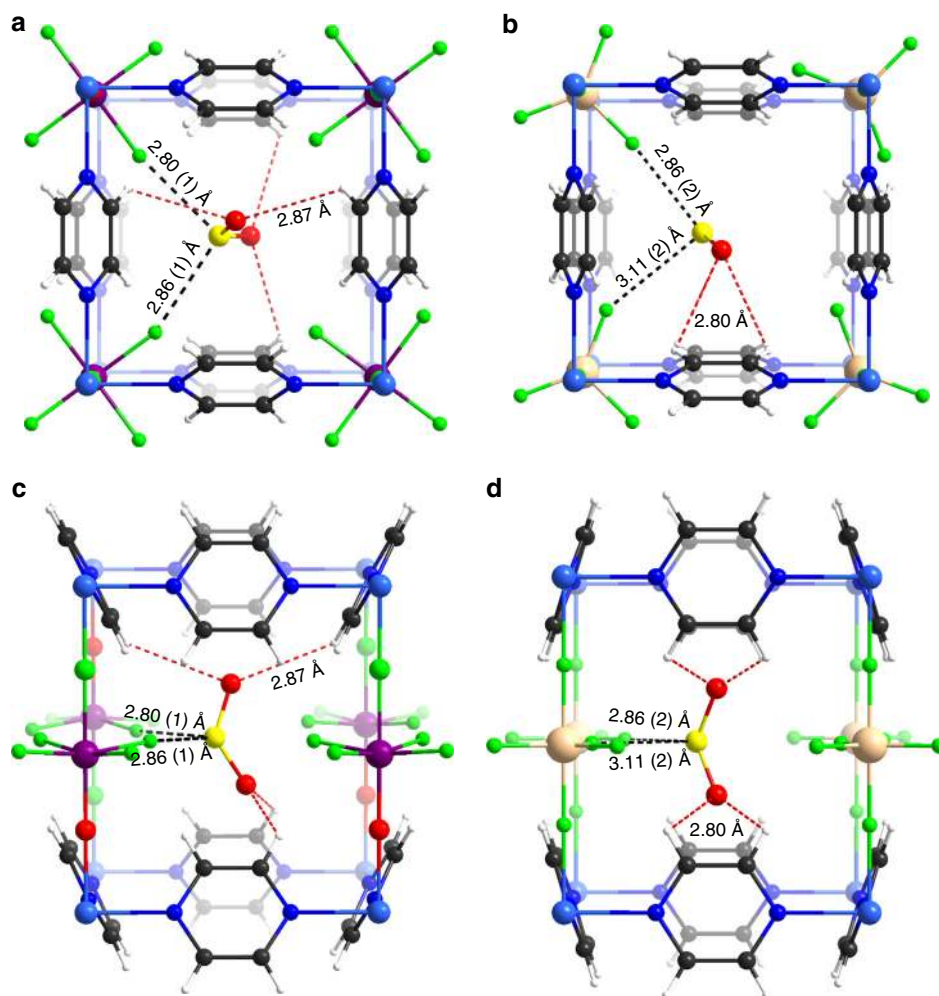**Fig. 2** In situ visualization of SO_2 in host frameworks. Intermolecular host–guest interactions in SO_2 loaded crystal structures of **a**, **c** KAUST-7 and **b**, **d** KAUST-8

bonds of the same anion are directed $\pm 24.1(4)°$ out the diagonal direction, and in the fourth channel there are no F-atoms from this pillar (Supplementary Figure 9a). Therefore, the single average cage aperture is formed by fluorine atoms of three adjacent $(AlF_5)^{2-}$ anions only. The pillar twist is stabilized by three pairs of C–H⋯F hydrogen bonds between the pyrazine molecules and the fluorine atoms with H⋯F distances and C–H⋯F angles of 2.38 Å and 178°, 2.48 Å and 134°, and 2.17 Å and 161°, respectively (Supplementary Figure 9b and 9c). Similar to SO_2-loaded KAUST-7 structure, the guest SO_2 molecule is disordered in the center of the 1D channel (the special position symmetry is $4/mmm$) of the KAUST-8 MOF. The distances between electropositive sulfur atom of the SO_2 molecule and fluorine atoms of adjacent F-pillars equals 2.86(2), 3.11(2), or 3.25 (1) Å depending on the $(AlF_5)^{2-}$ orientation ($\varphi = 0°$ or ± 24.1 (4)°, Supplementary Figure 9d) and each of them is less than the sum of the S and F van der Waals radii (3.27 Å). Contrary to the KAUST-7 structure, the SO_2 molecule participates in four C–H⋯O contacts with only two neighboring pyrazines (H⋯O distance = 2.80 Å, angle = 105°). These observations were supported by DFT calculations and it revealed a lowering of the host/guest interaction energy of CO_2 for KAUST-8 compared with KAUST-7 (-47.0 kJ mol^{-1} vs. -54.5 kJ mol^{-1}). In the case of KAUST-8, the trigonal bipyramidal-like Al^{3+} environment does not allow for further optimal interactions between a carbon atom in CO_2 and four F-pillars (Supplementary figure 3d), as seen

in KAUST-7. DFT calculations were further performed starting with the SO_2-loaded crystal structure model elucidated from SCD data. Interestingly, the simulated preferential location of SO_2 is slightly pushed toward the pore wall, as compared with the scenario in KAUST-7, with the formation of a dual interaction between its sulfur atoms and the two nearby F-pillars, as well as its oxygen atoms interacting with the pyrazine linker with shorter interacting distances (Supplementary Figure 3c). The resulting geometry led to a slight enhancement of the SO_2/host interaction energy (-73.9 kJ mol^{-1}) and reduced affinity toward CO_2, making KAUST-8 a promising candidate to selectively adsorb SO_2 over CO_2.

Investigation of single component SO_2 adsorption showed that KAUST-8 also exhibits steep adsorption isotherm at 25 °C (Supplementary Figure 10). The corresponding adsorption column breakthrough experiment with SO_2/N_2: 7/93 mixture showed a higher uptake of 2.2 mmol g^{-1} (Fig. 4a). KAUST-8 can be completely regenerated by heating at 105 °C in a vacuum or inert gas environment (Supplementary Figure 11), confirming SO_2 stability and recyclability. During the adsorption column breakthrough experiments carried out with low SO_2 (SO_2/N_2: 0.05/99.95) mixture, KAUST-8 still maintained a high uptake of SO_2 (1.6 mmol g^{-1}) (Fig. 4b, Supplementary Table 3). Subsequent TPD analysis of the adsorbed phase confirmed the adsorption of SO_2 (Supplementary Figure 12) at p.p.m. level. Supplementary Table 3 compares SO_2 uptake of different benchmark MOFs at
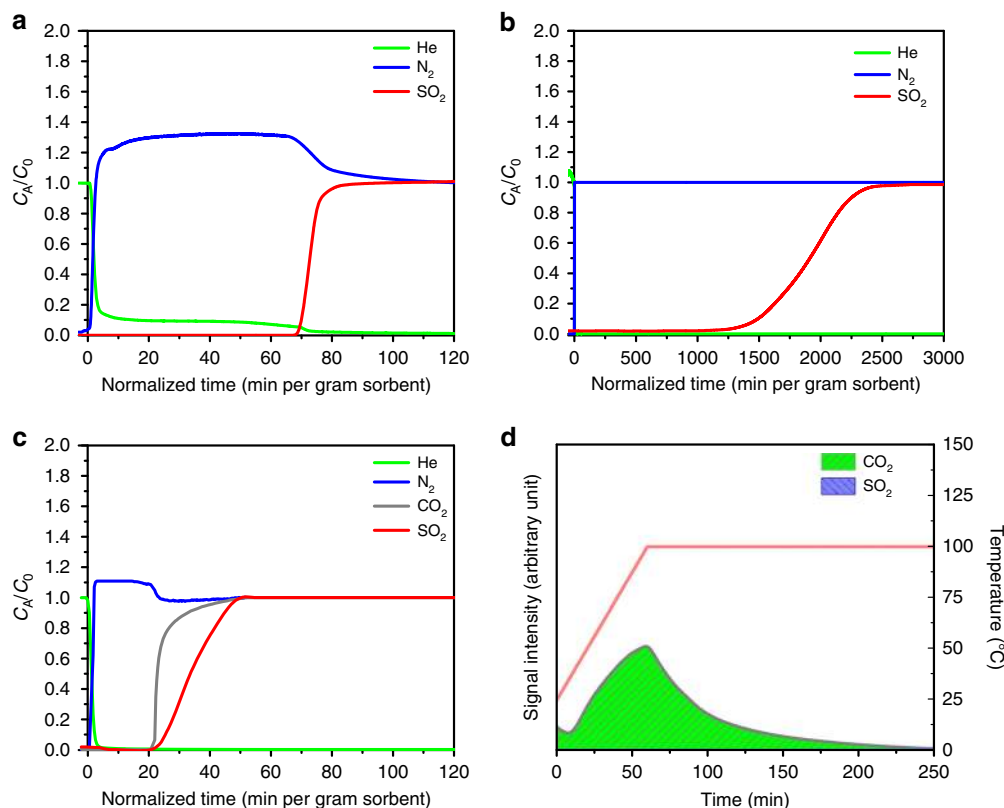
Fig. 3 CO_2/SO_2 capture performance of KAUST-**7**. Adsorption column breakthrough experiments for KAUST-**7** with **a** SO_2/N_2: 7/93 mixture (10 cm^3 min^{-1}, flow rate), **b** SO_2/N_2: 0.05/99.95 mixture (40 cm^3 min^{-1}, flow rate), and **c** $SO_2/CO_2/N_2$: 0.05/10/89.95 mixture (25 cm^3 min^{-1}, flow rate). **d** Temperature-programmed desorption after initial adsorption in the column using a mixture akin to flue gas ($SO_2/CO_2/N_2$: 0.05/10/89.95), suggesting an adsorbed phase composition dominated by CO_2

low concentration. Materials with relatively more open structure such as MFM-300(In, Al) have very high SO_2 uptake at higher SO_2 concentration; however, they have lower SO_2 uptake at lower concentrations close to 500 p.p.m. (of interest for application such as SO_2 capture from flue gas and SO_2 sensing) compared with KAUST-7, KAUST-8, and some SIF_6^{2-} based MOFs. Materials such as MFM-300(In, Al) with very high SO_2 uptake at higher SO_2 concentration could have many important applications. MFM-300(In, Al) (very high uptake at higher concentration), and KAUST-7 and KAUST-8 (high uptake at very low concentration) are complementary to each other and their uses depend upon nature of the application. Adsorption column breakthrough experiments with synthetic flue gas using a $SO_2/CO_2/N_2$: 0.05/10/89.95 mixture showed that SO_2 continues to be adsorbed for long durations past the CO_2 breakthrough time (Fig. 4c). This indicates that the adsorbed CO_2 is replaced by SO_2 from the gas mixture, which is consistent with a much higher estimated interaction energy of SO_2 over CO_2. Subsequent TPD analysis suggests an adsorbed phase composition of 1.5 mmol g^{-1} for CO_2 and 0.5 mmol g^{-1} for SO_2, which is remarkable considering the large difference in concentrations of CO_2 and SO_2 in the synthetic flue gas (Fig. 4d). A selectivity of $SO_2/CO_2 \approx 66$ obtained from the combination of breakthrough and TPD experiment shows that KAUST-8 is a highly efficient material for SO_2 removal at a p.p.m. level and is promising for selectively removing SO_2 from flue gas. The performance of KAUST-8 using humid (≈40% RH) 250 p.p.m. SO_2/ balance N_2 gas mixture was also investigated (Supplementary Figure 13). For KAUST-8, also SO_2 has almost the same breakthrough time as that of water; however, owing to its higher water adsorbing capacity than KAUST-7, it can adsorb more SO_2 compared with KAUST-7 under the same conditions.

Uptake of SO_2 by KAUST-8 in humid condition is notable considering in the above experiment gas stream contained almost 50 times higher concentration of water than SO_2. In addition to previously reported excellent water stability[46], SO_2 stability of the KAUST-8 was proven by PXRD comparison of the materials before and after dry and humid SO_2 exposure (Supplementary Figure 14), CO_2 breakthrough study before and after 7% SO_2 breakthrough experiments (Supplementary Figure 15) and CO_2 adsorption isotherm after the humid SO_2 breakthrough experiment (Supplementary Figure 16).

Selective SO_2 detection from air. From the adsorptive separation study above, KAUST-8 and KAUST-7 were shown to exhibit tunable CO_2/H_2S selectivity, molecules that are present in environments contaminated with SO_2. To benefit from the outstanding properties of this platform, we found it compelling to explore the feasibility of depositing KAUST-8 and KAUST-7 on a QCM electrode and unveiling their SO_2 sensing properties in the presence and absence of humidity to mimic atmospheric conditions. Weight-detectable sensor such as QCM has been used in this study to detect SO_2 accurately when the disturbing presence of moisture is involved. These imply that QCM device can be an alternative to IDE[48] when testing for a gas in the presence of humidity. Part of the reason for this difference is that IDE sensors are based on the change in dielectric constant ($\varepsilon_{H2O} = 80$ and $\varepsilon_{SO2} = 16$) and in order to detect SO_2 accurately in the presence of moisture the deposited materials on the IDE-type electrode has to overcome the high dielectric constant for H_2O.

The surface morphology of KAUST-8 and KAUST-7 coated on QCM (see inset) was studied using scanning electron microscopy.
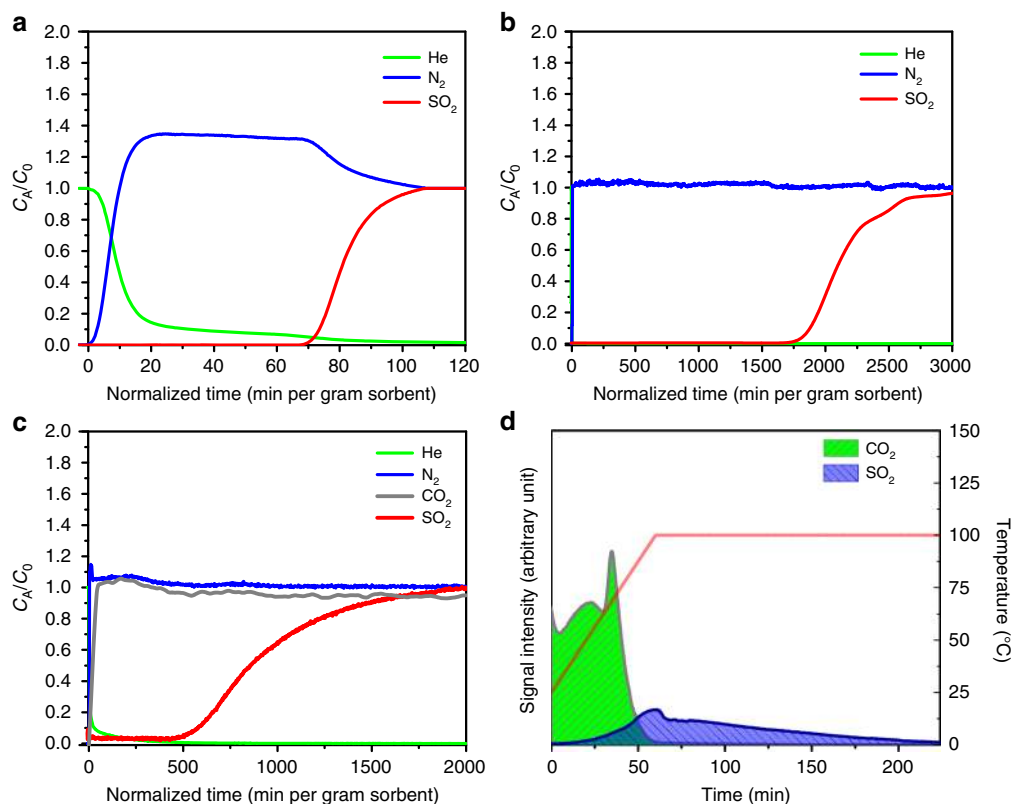
Fig. 4 CO_2/SO_2 capture performance of KAUST-8. Adsorption column breakthrough experiments for KAUST-8 with **a** SO_2/N_2: 7/93 (10 cm^3 min^{-1}, flow rate), **b** SO_2/N_2: 0.05/99.95 mixture (40 cm^3 min^{-1}, flow rate), and **c** $SO_2/CO_2/N_2$: 0.05/10/89.95 (40 cm^3 min^{-1}, flow rate). **d** TPD experiment suggests a considerable amount of SO_2 along with CO_2 as adsorbed phase after a breakthrough experiment with 500 p.p.m. SO_2 in the presence of 10% CO_2 and balance N_2
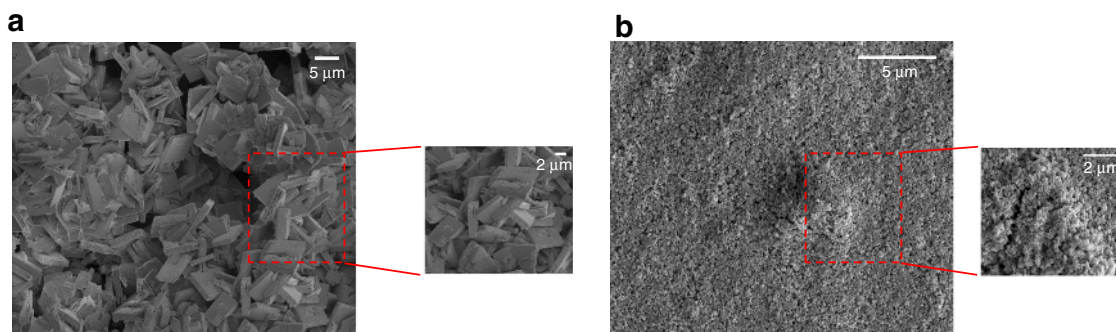

Fig. 5 Scanning electron microscopy of thin films. SEM micrographs at a high and low magnification of **a** KAUST-7 and **b** KAUST-8 thin films coated on the gold electrode of QCM

The thin films of both MOFs were found to be compact and uniform. The densely packed MOFs crystals were uniformly deposited on the QCM substrate with low intergranular voids and random orientation. As illustrated in Fig. 5, the coating of KAUST-7 led to cubic crystallites of ~150 nm, whereas for the KAUST-8 films the size of the crystallites is significantly larger at ~30 μm. PXRD experiments were carried out to confirm the purity and crystallinity of the deposited MOFs (Supplementary Figure 17).

The sensitivity ($\Delta f/f$) of KAUST-8- and KAUST-7-coated QCM devices were measured for different concentrations of SO_2, ranging from 0 to 500 p.p.m. in balance with nitrogen[18]. Uncoated QCM showed a negligible response to SO_2. With the increase in the concentration of SO_2, both MOF-coated sensors

responded with a nonlinear decrease in sensitivity (Fig. 6) and (Supplementary Figure 18). The lowest detection limit, defined theoretically using a largely accepted methodology by the sensing community[42], was estimated to be about 100 p.p.b. (with noise drift in the resonance frequency of ± 1.5 Hz)[49]. By optimizing the device parameters, drift in the sensors resonance frequency, this detection limit can be reduced to below 0.2 Hz[50,51] and thereby improving the detection limit to < 15 p.p.b. This discrepancy/ gap between the theoretical and experimental detection limits (15 p.p.b. and 5 p.p.m.) was never discussed previously in the open literature.

After each exposure cycle, the device was in situ heated at 105 °C in ambient nitrogen for 4 h, allowing the reactivation of the evaluated MOF thin film for another sensing cycle.

Humidity is present in most environments, and so it is important to understand a sensors response in its presence. Therefore, mixed gas experiments were performed, exposing KAUST-7 and KAUST-8 to SO_2 in humid conditions mimicking real-world conditions for SO_2 detection. Figure 7 shows the

sensor sensitivity as a function of SO_2 concentration in humid conditions (60% RH) at RT for uncoated and coated KAUST-7 and KAUST-8 QCMs. Uncoated QCM has a near-zero response to humidity and SO_2. This corroborates that the sensing response to SO_2 under humid conditions is due to its affinity to KAUST-7 and KAUST-8 films.

The responses of the two kinds of sensors were different. As seen in Fig. 7 and (Supplementary Figure 19), the resonance frequency of the QCMs initially decreased when the ambience was changed from dry to humid SO_2 conditions. The most prominent difference is the inversion in the sensor output due to the introduction of SO_2 at 60% RH but not in the same manner as compared with the dry SO_2 case. Interestingly, when exposed to 25 p.p.m. of SO_2 in the above-mentioned humid conditions, the sensor resonance frequency for SO_2 was reduced. Under humid conditions, the sensitivity of the two MOFs slightly reduced when compared with dry conditions. However, KAUST-7 films demonstrated a four-time higher sensitivity toward SO_2 in the presence of humidity compared with KAUST-8.

To further analyze the results obtained, it is necessary to consider the specific features of the adsorption of SO_2 and water on the surface of KAUST-7 and KAUST-8. As seen in Fig. 7, the presence of humidity (60% RH) did not significantly affect the KAUST-7-based sensors response to the SO_2 analyte. This may be due to the affinity of SO_2 molecules to replace some of the adsorbed water molecules or/and coexist in the highly confined pore system. In the case of KAUST-8-based sensor, which is isomorphic to the KAUST-7, lower sensitivity to SO_2 in the presence of humidity was observed. Although SO_2 has the affinity to replace water molecules, the reduced sensitivity is attributed to the absence of accessible ultra-microporous morphology. The number of SO_2-adsorbing active sites is reduced by the pre-adsorbed water, thereby limiting the available space in the pore system for adsorption. This observation is supported by the fact that the water molecules strongly interact with Al^{3+}[46] with higher host/guest interaction energy as compared with SO_2. The TPD experiment results (Supplementary Figure 20) show that in the case of KAUST-7, the SO_2 can replace the already adsorbed water molecules relatively easy as compared with the KAUST-8, which has stronger water affinity. These results are in agreement with the conclusion reported in the literature for the simultaneous capture of CO_2 and H_2O using KAUST-8[46].

The most important parameters for a sensing device are its stability and reproducibility. These parameters were investigated by cyclic exposure of the sensor to different SO_2 concentrations after every 48 h at RT over a period of 12 days (Fig. 8). The three results demonstrated the stability of the sensors exposed to 50, 100, and 157 p.p.m. SO_2 gas with no significant change in the resonant frequency over time.
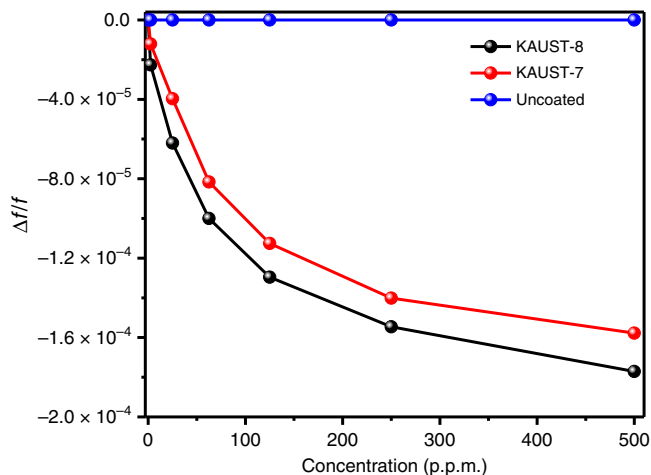

Fig. 6 Frequency shift comparisons. Frequency shift as a function of the SO_2 concentration for the uncoated and KAUST-7- or KAUST-8-coated QCM sensors
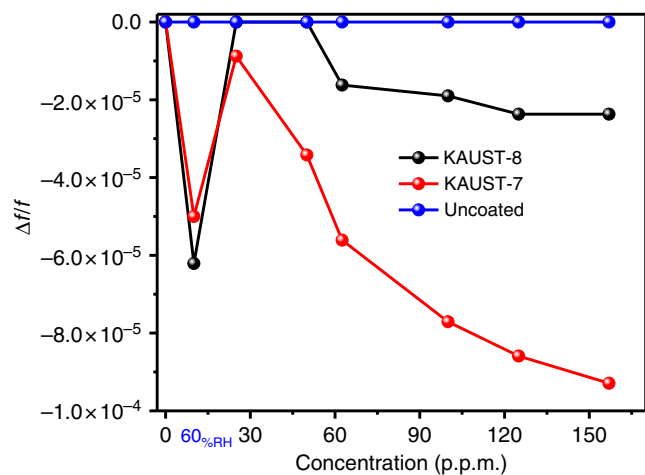

Fig. 7 Sensor responses. Plots of sensors responses as a function of SO_2 concentration in synthetic air
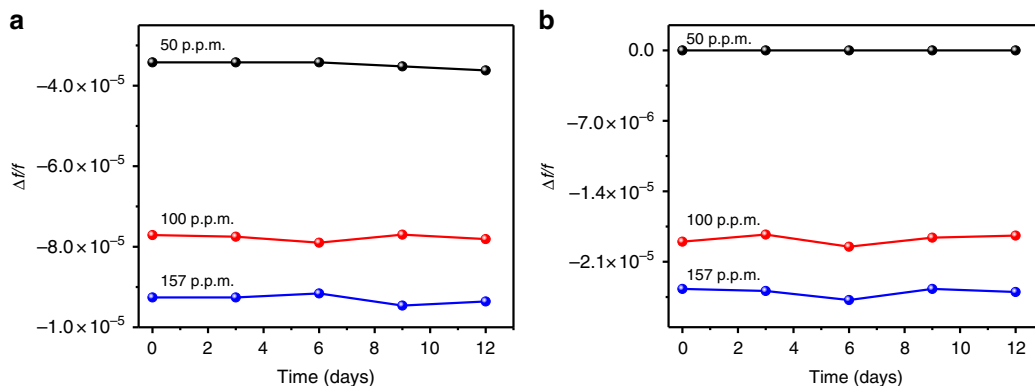

Fig. 8 Stability and reproducibility. Long-term stability property of the **a** KAUST-7 and **b** KAUST-8 sensors exposed to 50, 100, and 157 p.p.m. SO_2 gas

Discussion

In this report, we successfully demonstrated the superior performance of two fluorinated MOFs, namely KAUST-7 and KAUST-8, for the capture of SO_2 from flue gas. Combined mixed gas breakthrough experiments and molecular simulation confirmed that simultaneous capture of SO_2 and CO_2 occurs using KAUST-7, whereas KAUST-8 displays a higher affinity for SO_2 with SO_2/CO_2 selectivity ≈66. Based on this performance, QCM-based sensors were successfully fabricated for sensing SO_2 from air using this fluorinated MOF platform (Supplementary Figure 21). Both MOF materials confirmed their potential, revealing good SO_2 detection capabilities above 25 p.p.m., the range of SO_2 concentrations in the air-inducing nose and eye irritation. This remarkable performance of sensing makes these materials highly desirable for the fabrication of new advanced devices to improve health and environmental conditions.

Methods

Materials. All reagents were used as received from commercial suppliers without further purification.

KAUST-7[44,45] and KAUST-8[46] were synthesized according to literature procedures.

Powder X-ray diffraction. The PXRD data were collected over the 2θ range 4–40° or 6–80° on a high-resolution PANalytical X'Pert MPD-PRO diffractometer with Cu $K\alpha_1$ radiation ($\lambda = 1.5406$ Å, 45 kV/40 mA).

Single crystal X-ray diffraction. The SCXRD data were collected using a Bruker X8 PROSPECTOR APEX2 CCD diffractometer (Cu $K\alpha$, $\lambda = 1.54178$ Å). Indexings were performed using APEX2 (Difference Vectors method)[52]. Data integration and reduction were performed using SaintPlus[53]. Absorption corrections were performed by multi-scan method implemented in SADABS[54]. Space groups were determined using XPREP implemented in APEX2[52]. Both structures were solved using Direct Methods (SHELXS-97) and refined using SHELXL-2018/3 (full-matrix least-squares on F^2) contained WinGX v1.70.01[55–57].

In situ gas loading experiment. We used commercially available Swagelok miniature quick connect with a small modification that allowed us to fix 0.3 mm glass capillary loaded with crystal above the quick connect. The selected single crystal was glued to glass fiber and placed in 0.3 mm glass capillary before attaching it to quick connect. In situ pretreatment of the crystal loaded in environmental gas cell was carried out first under dry nitrogen flow. Temperature of the crystal increased by immersing the capillary into oil bath. Temperature of the oil bath was fixed at 140 °C for both the samples to obtain 105–120 °C effective temperature at the crystal. After 24 h, nitrogen flow was changed to dynamic vacuum keeping the temperature constant. After 12 h, crystal was allowed to cool down under dynamic vacuum and then 7% SO_2 (93% N_2) was introduced into environmental cell at 4–5 bar pressure. In case of CO_2, 100% CO_2 was introduced at 2–3 bar. The gas-loaded environmental cell was detached under pressure and allowed to equilibrate for around 8 h. After 8 h, the environmental cell was mounted on a modified goniometer for single crystal X-ray data collection.

Column breakthrough test set-up, procedure, and measurements. The experimental setup used for dynamic breakthrough measurements is shown in Supplementary Figure 22. The gas manifold consisted of three lines fitted with mass flow controllers. Line A is used to feed an inert gas, most commonly helium, to activate the sample before each experiment. The other two lines B and C feed a pure or pre-mixed gases. Whenever required, gases flowing through lines B and C may be mixed before entering a column packed with the sample using a four-way valve. In a typical experiment, 300–500 mg of adsorbent (in the column) was treated in situ at a required temperature under He flow (50 cm^3 g^{-1}) for 8 h.

Before starting each experiment, helium reference gas is flushed through the column and then the gas flow is switched to the desired gas mixture at the same flow rate between 10–50 cm^3 g^{-1}. The gas mixture downstream the column was monitored using a Hiden mass spectrometer.

Fabrication of KAUST-7- and KAUST-8-coated QCM. The transducer was a 10 MHz AT-cut piezoelectric QCM device with a thickness shear mode and placed between two gold electrodes for electrical connection. The QCM is rinsed with ethanol and dried in air. MOFs paste was then applied to the electrode of QCMs by spin-coating method (2 μm thick); no prior modification of the sensors surface was required.

The QCM sensor was then fixed in a sealed chamber. Before measurements, the fresh coated MOFs film was activated in situ for 4 h to have a guest free framework.

The resulting coatings are ultrathin and reproducible so that the stress upon absorption of SO_2 inducing a change in the mass change of the thin film is effective.

Sensing apparatus. Supplementary Figure 23 shows the sensing setup used in this study for real-time measurement. All the sensor measurements were carried out at RT, under a dry air total stream of 200 cm^3 m^{-1}. MFCs (mass flow controllers) from Alicat Scientific, Inc. were used to control the flow rate for gases coming from certified bottles. Stainless steel delivery lines or perfluoroalkoxy alkane, Perfluoroalkoxy (PFA) tubing (in regions requiring flexibility and resistivity to volatile organic compounds (VOCs)) were used on the setup with Vernier metering valves (from Swagelok) as a flow regulator. To detect the change in humidity level inside the chamber, a commercial humidity sensor (Honeywell HIH-4000–003) was used as a reference, which has an error < 0.5% RH. The QCM sensor was exposed to the analyte stream until a stable response was obtained; a two-port network (Keysight E5071C ENA) circuit was used to monitor the change in resonance frequency. A LabVIEW interface was used for synchronization and data acquisition by controlling the LCR meter (L = Inductance, C = Capacitance, R = Resistance) and the multimeter. Hence, the possibility of data loss was minimized.

Computational methods. All simulations were performed using the codes available in the Quantum Espresso package[58], which implements the DFT under periodic boundary conditions with planewave functions as basis sets[59]. The geometry optimizations were performed with the generalized gradient approximation (Perdew-Burke-Ernzerhof (PBE)[60] including the dispersion corrections described by the Grimme's scheme[61], maintaining fixed the atomic coordinates of the F-Ni-F chains and the unit cell dimensions. The relative ion positions were relaxed until all of the force components were lower than 0.001 Ry Bohr^{-1}. The equilibrium atomic positions of all systems were found by minimizing the total energy gradient. The ion cores were described by Vanderbilt ultrasoft pseudopotential[62] and the Kohn–Sham one-electron states were expanded in a planewave basis set with a kinetic cutoff energy of 50 Ry (500 Ry for the density) All the calculations were performed at the Γ-point. The Hubbard approach was also applied in order to better describe the localized d states of nickel. The Hubbard parameters (U) were taken from the calculations of Wang et al.[63], with a value of 6.4 eV for nickel. The Marzari–Vanderbilt smearing technique was used[64] with a broadening of 0.005 Ry in order to smooth the Fermi distribution.

The geometry optimizations of SO_2 and CO_2 in both MOFs were performed by considering one guest molecule per formula unit. The interaction energy was then calculated using the following equation: $\Delta E = E_{MOF/guest\ molecule} - E_{guest\ molecule} - E_{empty\ MOF}$, where $E_{MOF/guest\ molecule}$, $E_{guest\ molecule}$, and $E_{empty\ MOF}$ are the total energy of the loaded system (guest molecule + MOF), of the guest molecule and the single-point total energy of the MOF, respectively.

Data availability

The X-ray crystallographic data for KAUST-7 (SO_2) and KAUST-8 (SO_2) have been deposited at the Cambridge Crystallographic Data Centre (CCDC), under deposition numbers 1871683 and 1871684, respectively. These data can be obtained free of charge from the CCDC via www.ccdc.cam.ac.uk. All other relevant data supporting the findings of this study are available from the corresponding authors on request.

References

1. Adil, K. et al. Valuing metal–organic frameworks for postcombustion carbon capture: a benchmark study for evaluating physical adsorbents. *Adv. Mater.* **29**, 1702953 (2017).

2. Rezaei, F., Rownaghi, A. A., Monjezi, S., Lively, R. P. & Jones, C. W. SO_x/NO_x removal from flue gas streams by solid adsorbents: a review of current challenges and future directions. *Energy Fuels* **29**, 5467–5486 (2015).

3. Ryu, H.-J., Grace, J. R. & Lim, C. J. Simultaneous CO_2/SO_2 capture characteristics of three limestones in a fluidized-bed reactor. *Energy Fuels* **20**, 1621–1628 (2006).

4. Clarke, A. G. & Radojevic, M. Oxidation of SO_2 in rainwater and its role in acid rain chemistry. *Atmos. Environ. (1967)* **21**, 1115–1123 (1987).

5. Galloway, J. N., Dianwu, Z., Jiling, X. & Likens, G. E. Acid rain: China, United States, and a remote area. *Science* **236**, 1559–1562 (1987).

6. Berger, F., Fromm, M., Chambaudet, A. & Planade, R. Tin dioxide-based gas sensors for SO_2 detection: a chemical interpretation of the increase in sensitivity obtained after a primary detection. *Sens. Actuators B Chem.* **45**, 175–181 (1997).

7. Torvela, H., Huusko, J. & Lantto, V. Reduction of the interference caused by NO and SO_2 in the CO response of Pd-catalysed SnO_2 combustion gas sensors. *Sens. Actuators B Chem.* **4**, 479–484 (1991).

8. Shimizu, Y., Matsunaga, N., Hyodo, T. & Egashira, M. Improvement of SO$_2$ sensing properties of WO$_3$ by noble metal loading. *Sens. Actuators B Chem.* **77**, 35–40 (2001).

9. Stankova, M. et al. Detection of SO$_2$ and H$_2$S in CO$_2$ stream by means of WO3-based micro-hotplate sensors. *Sens. Actuators B Chem.* **102**, 219–225 (2004).

10. Penza, M., Cassano, G. & Tortorella, F. Gas recognition by activated WO$_3$ thin-film sensors array. *Sens. Actuators B Chem.* **81**, 115–121 (2001).

11. Gardon, M. & Guilemany, J. M. A review on fabrication, sensing mechanisms and performance of metal oxide gas sensors. *J. Mat. Sci. Mater. Electron.* **24**, 1410–1421 (2013).

12. Barsan, N., Koziej, D. & Weimar, U. Metal oxide-based gas sensor research: How to? *Sens. Actuators B Chem.* **121**, 18–35 (2007).

13. Williams, D. E. Semiconducting oxides as gas-sensitive resistors. *Sens. Actuators B Chem.* **57**, 1–16 (1999).

14. Korotcenkov, G. Metal oxides for solid-state gas sensors: what determines our choice? *Mater. Sci. Eng. B* **139**, 1–23 (2007).

15. Hübert, T., Boon-Brett, L., Black, G. & Banach, U. Hydrogen sensors – a review. *Sens. Actuators B Chem.* **157**, 329–352 (2011).

16. Yan, Y., Wladyka, C., Fujii, J. & Sockanathan, S. Prdx4 is a compartment-specific H$_2$O$_2$ sensor that regulates neurogenesis by controlling surface expression of GDE2. *Nat. Commun.* **6**, 7006 (2015).

17. Awang, Z. Gas sensors: a review. *Sens. Transducers* **168**, 61–75 (2014).

18. Chappanda, K. N. et al. The quest for highly sensitive QCM humidity sensors: the coating of CNT/MOF composite sensing films as case study. *Sens. Actuators B Chem.* **257**, 609–619 (2018).

19. Li, J.-R., Kuppler, R. J. & Zhou, H.-C. Selective gas adsorption and separation in metal–organic frameworks. *Chem. Soc. Rev.* **38**, 1477–1504 (2009).

20. Bhatt, P. M. et al. Isoreticular rare earth fcu-MOFs for the selective removal of H$_2$S from CO$_2$ containing gases. *Chem. Eng. J.* **324**, 392–396 (2017).

21. Cui, X. et al. Ultrahigh and selective SO$_2$ uptake in inorganic anion-pillared hybrid porous materials. *Adv. Mater.* **29**, 1606929 (2017).

22. Kreno, L. E. et al. Metal–organic framework materials as chemical sensors. *Chem. Rev.* **112**, 1105–1125 (2011).

23. Mohideen, M. I. H. et al. A fine-tuned MOF for gas and vapor separation: a multipurpose adsorbent for acid gas removal, hehydration, and BTX sieving. *Chem* **3**, 822–833 (2017).

24. AbdulHalim, R. G. et al. A fine-tuned metal–organic framework for autonomous indoor moisture control. *J. Am. Chem. Soc.* **139**, 10715–10722 (2017).

25. Tansell, A. J., Jones, C. L. & Easun, T. L. MOF the beaten track: unusual structures and uncommon applications of metal–organic frameworks. *Chem. Cent. J.* **11**, 100 (2017).

26. Adil, K. et al. Gas/vapour separation using ultra-microporous metal–organic frameworks: insights into the structure/separation relationship. *Chem. Soc. Rev.* **46**, 3402–3430 (2017).

27. Yang, S. et al. Selectivity and direct visualization of carbon dioxide and sulfur dioxide in a decorated porous host. *Nat. Chem.* **4**, 887–894 (2012).

28. Mathew, S. et al. Selective adsorption of sulfur dioxide in a robust metal–organic framework material. *Adv. Mater.* **28**, 8705 (2016).

29. Rodríguez-Albelo, L. M. et al. Selective sulfur dioxide adsorption on crystal defect sites on an isoreticular metal organic framework series. *Nat. Commun.* **8**, 14457 (2017).

30. Rad, A. S. & Chourani, A. Nickel based paddle-wheel metal–organic frameworks towards adsorption of O$_3$ and SO$_2$ molecules: quantum-chemical calculations. *J. Inorg. Organomet. Polym. Mater.* **27**, 1826–1834 (2017).

31. Lee, G.-Y. et al. Amine-functionalized covalent organic framework for efficient SO$_2$ capture with high reversibility. *Sci. Rep.* **7**, 557 (2017).

32. Glomb, S., Woschko, D., Makhloufi, G. & Janiak, C. Metal–organic frameworks with internal urea-functionalized dicarboxylate linkers for SO$_2$ and NH$_3$ adsorption. *ACS Appl. Mater. Interfaces* **9**, 37419–37434 (2017).

33. Fernandez, C. A. et al. Gas-induced expansion and contraction of a fluorinated metal−organic framework. *Cryst. Growth Des.* **10**, 1037–1039 (2010).

34. Tan, K. et al. Mechanism of preferential adsorption of SO$_2$ into two microporous paddle wheel frameworks M(bdc)(ted)$_{0.5}$. *Chem. Mater.* **25**, 4653–4662 (2013).

35. Thallapally, P. K., Motkuri, R. K., Fernandez, C. A., McGrail, B. P. & Behrooz, G. S. Prussian blue analogues for CO$_2$ and SO$_2$ capture and separation applications. *Inorg. Chem.* **49**, 4909–4915 (2010).

36. Yang, S. et al. Irreversible network transformation in a dynamic porous host catalyzed by sulfur dioxide. *J. Am. Chem. Soc.* **135**, 4954–4957 (2013).

37. Zhang, D., Wu, J., Li, P. & Cao, Y. Room-temperature SO$_2$ gas-sensing properties based on a metal-doped MoS$_2$ nanoflower: an experimental and density functional theory investigation. *J. Mat. Chem. A* **5**, 20666–20677 (2017).

38. Zhang, D., Liu, J., Jiang, C. & Li, P. High-performance sulfur dioxide sensing properties of layer-by-layer self-assembled titania-modified graphene hybrid nanocomposite. *Sens. Actuators B: Chem.* **245**, 560–567 (2017).

39. Sasaki, I., Tsuchiya, H., Nishioka, M., Sadakata, M. & Okubo, T. Gas sensing with zeolite-coated quartz crystal microbalances—principal component analysis approach. *Sens. Actuators B: Chem.* **86**, 26–33 (2002).

40. Osada, M., Sasaki, I., Nishioka, M., Sadakata, M. & Okubo, T. Synthesis of a faujasite thin layer and its application for SO$_2$ sensing at elevated temperatures. *Microporous Mesoporous Mater.* **23**, 287–294 (1998).

41. Lee, S. C. et al. A novel tin oxide-based recoverable thick film SO$_2$ gas sensor promoted with magnesium and vanadium oxides. *Sens. Actuators B Chem.* **160**, 1328–1334 (2011).

42. Chernikova, V., Yassine, O., Shekhah, O., Eddaoudi, M. & Salama, K. N. Highly sensitive and selective SO$_2$ MOF sensor: the integration of MFM-300 MOF as a sensitive layer on a capacitive interdigitated electrode. *J. Mater. Chem. A* **6**, 5550–5554 (2018).

43. Sapsanis, C. et al. Insights on capacitive interdigitated electrodes coated with MOF thin films: Humidity and VOCs sensing as a case study. *Sensors* **15**, 18153–18166 (2015).

44. Bhatt, P. M. et al. A fine-tuned fluorinated MOF addresses the needs for trace CO$_2$ removal and air capture using physisorption. *J. Am. Chem. Soc.* **138**, 9301–9307 (2016).

45. Cadiau, A., Adil, K., Bhatt, P., Belmabkhout, Y. & Eddaoudi, M. A metal-organic framework–based splitter for separating propylene from propane. *Science* **353**, 137–140 (2016).

46. Cadiau, A. et al. Hydrolytically stable fluorinated metal-organic frameworks for energy-efficient dehydration. *Science* **356**, 731–735 (2017).

47. Belmabkhout, Y. et al. Natural gas upgrading using a fluorinated MOF with tuned H2S and CO2 adsorption selectivity. *Nature Energy* **3**, 1059–1066 (2018).

48. Zeinali, S., Homayoonnia, S. & Homayoonnia, G. Comparative investigation of interdigitated and Parallel-plate capacitive gas sensors based on Cu-BTC nanoparticles for selective detection of polar and apolar VOCs indoors. *Sens. Actuators B Chem.* **278**, 153–164 (2018).

49. Yamagiwa, H. et al. Detection of volatile organic compounds by weight-detectable sensors coated with metal-organic frameworks. *Sci. Rep.* **4**, 6247 (2014).

50. Rodriguez-Pardo, L., Rodríguez, J. F., Gabrielli, C., Perrot, H. & Brendel, R. Sensitivity, noise, and resolution in QCM sensors in liquid media. *IEEE Sens. J.* **5**, 1251–1257 (2005).

51. Cao-Paz, A. M., Rodríguez-Pardo, L., Fariña, J. & Marcos-Acevedo, J. Resolution in QCM sensors for the viscosity and density of liquids: application to lead acid batteries. *Sensors* **12**, 10604–10620 (2012).

52. APEX2 Ver. 2014.11-0, Bruker AXS, Inc., Madison, Wisconsin, USA, 2014.

53. SAINT Ver.8.34A. Bruker AXS, Inc., Madison, Wisconsin, USA, 2014.

54. SADABS Ver. 2014/15. Bruker AXS, Inc., Madison, Wisconsin, USA, 2014

55. SHELXS-97, Program for Crystal Structure Solution (Univ. Göttingen, Germany, 1997).

56. Sheldrick, G.M. SHELXL-2018/3. Crystal structure refinement with SHELXL. *Acta Cryst.* **C71**, 3–8 (2015).

57. WinGX. Farrugia, L. J. WinGX and ORTEP for Windows: an update. *J. Appl. Cryst.* **45**, 849–854 (2012).

58. Giannozzi, P. et al. QUANTUM ESPRESSO: a modular and open-source software project for quantum simulations of materials. *J. Phys. Condens. Matter* **21**, 395502 (2009).

59. Hohenberg, P. & Kohn, W. Inhomogeneous electron gas. *Phys. Rev.* **136**, B864 (1964).

60. Kohn, W. & Sham, L. J. Self-consistent equations including exchange and correlation effects. *Phys. Rev.* **140**, A1133 (1965).

61. Perdew, J. P., Burke, K. & Ernzerhof, M. Generalized gradient approximation made simple. *Phys. Rev. Lett.* **77**, 3865 (1996).

62. Vanderbilt, D. Soft self-consistent pseudopotentials in a generalized eigenvalue formalism. *Phys. Rev. B* **41**, 7892 (1990).

63. Wang, L., Maxisch, T. & Ceder, G. Oxidation energies of transition metal oxides within the GGA+ U framework. *Phys. Rev. B* **73**, 195107 (2006).

64. Marzari, N., Vanderbilt, D., De Vita, A. & Payne, M. Thermal contraction and disordering of the Al (110) surface. *Phys. Rev. Lett.* **82**, 3296 (1999).

Author contributions

K.A. and A.C. carried out the synthetic experiments. K.A. and M.R.T contributed to the conceptual approach in designing the MOF deposition on the electrode. G.D.W., N.H., and Y.B. set, conducted, and analyzed the single component SO$_2$ gas adsorption experiments. P.B. and Y.B. conducted and interpreted the column breakthrough experiments. A.S. and P.B. carried out in situ SO$_2$-loaded single crystal X-ray diffraction study and analysis. Y.B., M.R.T., and K.A. conceptualized the set of sensing testing. Y.B., M.R.T., K.A., K.N.S., and K.N.C. conducted and interpreted the sensing results. S.T and G.M performed the theoretical study. K.A., Y.B., and M.E. conceived, designed, and guided the whole project. P.B., M.R.T., Y.B., K.A., M.E., K.N.C., and A.S. wrote the manuscript and all authors approved it.

Additional information

Competing interests: The authors declare no competing interests.

Journal peer review information: *Nature Communications* thanks the anonymous reviewers for their contribution to the peer review of this work.

Publisher's note: Springer Nature remains neutral with regard to jurisdictional claims in published maps and institutional affiliations.